

## Multi-Point Shape Optimization of Airfoils at Low Reynolds Numbers

D.N. Srinath<sup>1</sup>, Sanjay Mittal<sup>1</sup> and Veera Manek<sup>2</sup>

**Abstract:** A continuous adjoint method is formulated and implemented for the multi-point shape optimization of airfoils at low  $Re$ . The airfoil shape is parametrized with a non-uniform rational B-Spline (NURBS). Optimization studies are carried out for two different objective functions. The first involves an inverse function on the lift coefficient over a range of  $Re$ . The objective is to determine a shape that results in a lift coefficient of 0.4 at three values of  $Re$  : 10, 100 and 500. The second objective involves a direct function on the lift coefficient over a range of angles of attack,  $\alpha$ . The lift coefficient is maximized simultaneously for  $\alpha = 4^\circ, 8^\circ$  and  $12^\circ$  while the  $Re$  is held constant. The final shapes from both the cases are compared with those from the single-point optimization at each of the operating point. It is seen that the multi-point shapes are significantly different. They also have a better off-design performance than the geometries from single-point designs.

**Keywords:** airfoils, multi-point, shape optimization, adjoint methods, low Reynolds numbers, finite element

### 1 Introduction

Optimization methods can be broadly classified as one of the two types: gradient and non-gradient based. In the gradient based methods, the gradient of a desired objective function with respect to the defined parameters is utilized to obtain a search direction. These methods are capable of finding only a local optima. The possibility of the local optima being a global one depends on the initial guess. Gradients have been computed via different methods in the past. Probably, the simplest method of evaluating the gradients is via using finite differences. In these methods the function to be minimized (or maximized) is perturbed by a small quantity. The gradient can then be computed by using a Taylor series expansion. These methods can become very expensive if the cost of computing the objective function is

---

<sup>1</sup> Dept. of Aerospace Engineering, IIT Kanpur, 208016, India

<sup>2</sup> Summer Intern, Dept. of Aerospace Engineering, IIT Kanpur, 208016, India

high. For example, if the objective function depends on the solution of the Navier-Stokes equations, then for  $n$  design parameters,  $n + 1$  flow computations would be required to obtain the gradient. Also, the magnitude of perturbation is problem specific and not known a priori. Other methods that have been developed to compute the gradient at reduced cost include the complex Taylor series expansion approach [Burg and Newman (2003)], automatic differentiation [Sherman, Taylor, Green, P.A. Newman, Hou, and Korivi (1994)], direct differentiation [Hou, Sheen, and Chuang (1992)] and adjoint based methods [M.B. Giles and Pierce (2000)]. For mixed complementarity problems, Liu and Atluri [Liu and Atluri (2008)] recently developed a method that converts the optimization problem into a set of nonlinear algebraic equations. They found that this approach provides accurate solutions and be easily extended to include constraints that involve nonlinear equalities as well as inequalities. Non-gradient based methods like genetic algorithms [Obyashi (1996)], on the other hand, use only the objective function to obtain an optima. They are capable of finding a global optima but are generally expensive because they require a large number of number of function evaluations.

Optimization, in the context of engineering applications, can be carried either on the topology or the shape [Bendsoe and Sigmund (2002)]. Topology optimization [Tapp, Hansel, Mittelstedt, and Becker (2004); Csilino (2006); Wang, Lim, Khoo, and Wang (2007); Liu and Atluri (2008)] deals with the determination of an optimal distribution of material within the design space of a structure while shape optimization involves determining the optimal shape of a given structure. Various methods have been employed to carry out topology optimization of structures. Some examples are: the homogenization approach [Bendsoe and Kikuchi (1988)], variable density approach [Bendsoe and Sigmund (1999)], evolutionary structural optimization approach [Zhou and Rozvany (2001)], and optimality criteria method [Juan, Shuyao, Yuanbo, and Guangyao (2008)]. In this work, we focus on shape optimization using an adjoint based method. Adjoint methods, for shape optimization, have been utilized in diverse areas such as aerospace [Mohammadi (2004); Kim, Alonso, and Jameson (2000)], marine [Soto, Lohner, and Yang (2004)] and bio-medical engineering [Abraham, Behr, and Heinkenschloss (2005)].

Aerodynamic design of airfoils by numerical methods has received much attention in recent years. Flow solvers are combined with an optimization method for this purpose. Adjoint based methods [Pironneau (1973, 1974); Jameson (1988); Mohammadi and Pironneau (2004); Okumura and Kawahara (2000)] have been popular for aerodynamic design because the cost of computing the gradient is independent of the number of design variables. Non-gradient based methods such as genetic algorithms [Obyashi (1996)], while being robust, are not preferred due to the large computational costs involved. Airfoil shape optimization has been car-

ried out by many researchers in the past [Anderson and Venkarakrishnan (1997); Soto, Lohner, and Yang (2004); Anderson and Bonhaus (1999); Kim, Alonso, and Jameson (2000)]. Progress has also been made in optimization of 3D wings [Brezillion and Gauger (2004); Elliot and Perraire (1997)]. However, almost all of these efforts find optimal shapes at one fixed operating condition. In practice, airfoils are expected to perform efficiently over a range of operating conditions. Shapes obtained by optimizing at one operating point, often, have poor off-design performance. One way of addressing this drawback is to include off-design conditions in the problem definition. This may be achieved via multi-point optimization methods where performance over a range of operating conditions is considered.

Drela [Drela (1998)] studied the behavior of an optimization cycle in the presence of a large number of design variables in two dimensions. He noticed that, in the presence of sufficient design mode resolution, improved performance is seen only near the design condition. The design from a single-point optimization tends to have severely degraded off-design performance. On this basis he suggested that for a multi-point problem increasing the number of design variables requires a corresponding increase in the number of operating (sampling) points. Since the cost of computing the optima increases with increase in number of sampling points, reducing the number of design variables to an absolute minimum is essential. Reducing the number of design variables also eliminates the possibility of the optimal shape being "noisy".

A popular method to solve multi-point optimization problems is the weighted-sum method [Nemec, Zingg, and Pulliam (2004)]. Different weights are assigned to each of the sampling points. The relative magnitude of the weights indicate the importance accorded to the respective sampling points. These weights are not known apriori and are often selected arbitrarily. Prior experience is required to estimate these weights. If appropriate weights are not assigned the optimal shape will most likely have sub-optimal performance. Also, optimal performance over a range of operating conditions requires selection of appropriate operating points. Again, these are unknown apriori. Zingg and Elias [Zingg and Elias (2006)] developed an automated procedure to appropriately select the operating points and their weights. In their method, depending on the performance over a range of operating conditions, additional sampling points are included. A few methods like the profile optimization method of Li et al. [Li, Huyse, and Padula (2002)] and the probabilistic approach of Huyse et al. [Huyse, Padula, Lewsi, and Li (2002)] can be utilized to optimize over a range of operating conditions.

Most of work done in multi-point optimization has been for high  $Re$  applications. The present work investigates multi-point optimization of airfoils at low  $Re$ . Two cases are considered. In the first case, an optimal airfoil that results in a specified lift

coefficient, over a range of Reynolds numbers, is sought. The second case involves obtaining an airfoil that achieves maximum lift coefficient, over a range of angles of attack, for a particular  $Re$ . The optimal airfoils from both the cases are compared with the shapes obtained from single-point optimization. The geometry of the airfoil is parametrized by a fourth order Non-Uniform Rational B-Splines (NURBS) curve [Farin (1990)]. A stabilized finite element method based on streamline-upwind Petrov/Galerkin(SUPG) and pressure stabilized Petrov/Galerkin(PSPG) [Tezduyar, Mittal, Ray, and Shih (1992)] stabilization techniques is employed to solve, both, the flow and adjoint equations. The Limited memory-Broyden-Fletcher-Goldfarb-Shanno (L-BFGS) algorithm [Byrd, Lu, Nocedal, and Zhu (1995)] is used to minimize the objective function.

## 2 Mathematical Formulation

### 2.1 Flow equations

Consider a domain  $\Omega$ , with boundary  $\Gamma$ , that is occupied by a fluid of density  $\rho$  and dynamic viscosity  $\mu$ . The governing equations for a steady incompressible flow of this fluid are given as:

$$\rho \mathbf{u} \cdot \nabla \mathbf{u} + \nabla \cdot \boldsymbol{\sigma} = \mathbf{0} \quad \text{on } \Omega \quad (1)$$

$$\nabla \cdot \mathbf{u} = 0 \quad \text{on } \Omega \quad (2)$$

where  $\mathbf{u}$  is the velocity and  $\boldsymbol{\sigma}$  the stress tensor. For a Newtonian fluid the stress tensor is given as  $\boldsymbol{\sigma} = -p\mathbf{I} + \mu[\nabla \mathbf{u} + (\nabla \mathbf{u})^T]$  where,  $p$  is the pressure and  $\mathbf{I}$  the identity tensor. The boundary conditions are either on the flow velocity or stress. Both, Dirichlet and Neumann type boundary conditions are accounted for:

$$\mathbf{u} = \mathbf{g} \quad \text{on } \Gamma_g \quad (3)$$

$$\mathbf{n} \cdot \boldsymbol{\sigma} = \mathbf{h} \quad \text{on } \Gamma_h \quad (4)$$

where,  $\mathbf{n}$  is the unit normal vector on the boundary  $\Gamma$ . Here,  $\Gamma_g$  and  $\Gamma_h$  are the subsets of the boundary  $\Gamma$ . More details on the boundary conditions are given in Figure 1. The drag and lift force,  $(D, L)$ , on the body can be calculated using the following expression:

$$(D, L) = \int_{\Gamma_B} \boldsymbol{\sigma} \mathbf{n} d\Gamma \quad (5)$$

where,  $\Gamma_B$  represents the surface of the body.

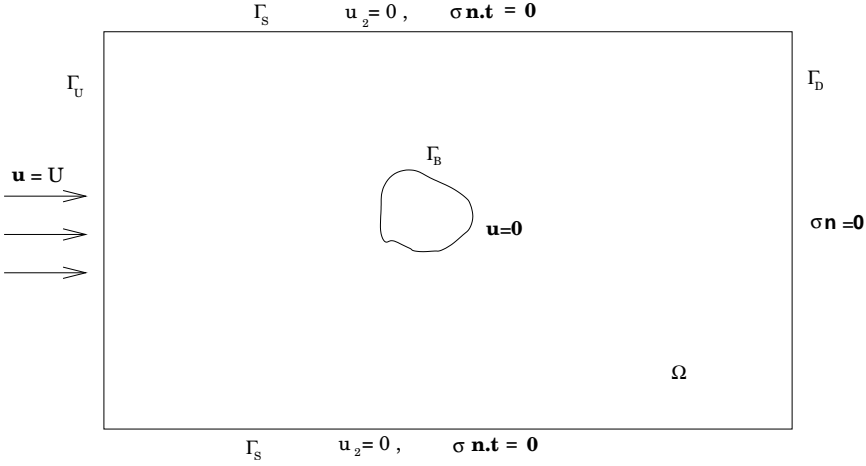


Figure 1: Schematic of the problem set-up: boundary conditions.  $\Gamma_U$ ,  $\Gamma_D$  and  $\Gamma_S$  are the upstream, downstream and lateral boundaries, respectively and  $\Gamma_B$  is the body surface.

## 2.2 The continuous adjoint approach

Let  $\Gamma_B$  be the segment of the boundary,  $\Gamma$ , whose shape is to be determined. Let  $\boldsymbol{\beta} = (\beta_1, \dots, \beta_m)$  be the set of shape parameters that govern its shape. Further, an objective function,  $I_c(\mathbf{U}, \boldsymbol{\beta})$ , is defined that depends on the flow variables  $\mathbf{U} = (\mathbf{u}, p)$  and shape parameters  $\boldsymbol{\beta}$ . The optimization problem involves determining the shape parameters that minimize (or maximize) the objective function,  $I_c(\mathbf{U}, \boldsymbol{\beta})$ . The flow equations (1) and (2) may be written as  $\mathfrak{K} = (\mathfrak{K}_u, \mathfrak{K}_p)$ , where  $\mathfrak{K}_u$  is the momentum equation and  $\mathfrak{K}_p$  the continuity equation. These equations appear as constraint conditions on the objective function,  $I_c(\mathbf{U}, \boldsymbol{\beta})$ , and have to be satisfied while  $I_c$  is minimized (or maximized). An augmented objective function is constructed to convert the constrained problem to an unconstrained one. The flow equations are augmented to the original objective function by introducing a set of Lagrange multipliers or adjoint variables,  $\boldsymbol{\Psi} = (\boldsymbol{\psi}_u, \boldsymbol{\psi}_p)$ .

$$I = I_c + \int_{\Omega} \boldsymbol{\Psi} \cdot \mathfrak{K} d\Omega \quad (6)$$

It can be noticed that the augmented objective function degenerates to the original one if the flow variables,  $\mathbf{U}$ , satisfy equations (1) and (2). The variation of the

augmented objective function is given as:

$$\delta I = \frac{\partial I}{\partial \mathbf{U}} \delta \mathbf{U} + \frac{\partial I}{\partial \boldsymbol{\beta}} \delta \boldsymbol{\beta} + \frac{\partial I}{\partial \boldsymbol{\Psi}} \delta \boldsymbol{\Psi}. \tag{7}$$

It is seen from Equation (7) that  $\delta I$  depends on variations of  $\mathbf{U}$ ,  $\boldsymbol{\beta}$  and  $\boldsymbol{\Psi}$ . These variations are given as:

$$\frac{\partial I}{\partial \boldsymbol{\Psi}} = \mathfrak{R}(\mathbf{U}, \boldsymbol{\beta}) \tag{8}$$

$$\frac{\partial I}{\partial \mathbf{U}} = \left( \frac{\partial I_c}{\partial \mathbf{U}} + \int_{\Omega} \boldsymbol{\Psi}^T \frac{\partial \mathfrak{R}}{\partial \mathbf{U}} d\Omega \right) \tag{9}$$

$$\frac{\partial I}{\partial \boldsymbol{\beta}} = \left( \frac{\partial I_c}{\partial \boldsymbol{\beta}} + \int_{\Omega} \boldsymbol{\Psi}^T \frac{\partial \mathfrak{R}}{\partial \boldsymbol{\beta}} d\Omega \right) \tag{10}$$

The optimal solution is achieved when the variation of the augmented objective function vanishes, i.e.,  $\delta I = 0$ . For this condition to be satisfied, each of the three expressions in equations (8)-(10) should go to zero. Equation (8) leads to the flow equations (1) and (2). Equation (9) results in the adjoint equations which can be utilized to compute the adjoint field. The gradient of the augmented objective function, as given by equation (10), quantifies the sensitivity of the objective function with respect to the design parameters. It is utilized to refine the direction of search of the optimal shape parameters. The optimal solution is obtained when the gradient approaches zero. More details on the computation of the adjoint equations are given in the next section.

### 2.3 Adjoint equations

The equations and boundary conditions for the adjoint variables are obtained by setting the expression given in Equation (9) to zero. This leads to:

$$\rho(\nabla \mathbf{u})^T \boldsymbol{\psi}_u - \rho(\mathbf{u} \cdot \nabla) \boldsymbol{\psi}_u - \nabla \cdot \boldsymbol{\sigma}_{\boldsymbol{\psi}} = \mathbf{0} \text{ on } \Omega \tag{11}$$

$$\nabla \cdot \boldsymbol{\psi}_u = 0 \text{ on } \Omega. \tag{12}$$

Here  $\boldsymbol{\sigma}_{\boldsymbol{\psi}}$  is similar to the stress tensor and is given by  $\boldsymbol{\sigma}_{\boldsymbol{\psi}} = -\psi_p \mathbf{I} + \mu[\nabla \boldsymbol{\psi}_u + (\nabla \boldsymbol{\psi}_u)^T]$ . The variables  $\boldsymbol{\psi}_u$  and  $\psi_p$  are referred to as the adjoint velocity and adjoint pressure, respectively. Unlike the flow equations the equations for the adjoint

variables are linear. The boundary conditions on the adjoint variables are:

$$\boldsymbol{\psi}_u = \mathbf{0} \text{ on } \Gamma_U \quad (13)$$

$$\mathbf{s} = \mathbf{0} \text{ on } \Gamma_D \quad (14)$$

$$s_1 = 0, \quad \psi_{u_2} = 0 \text{ on } \Gamma_S \quad (15)$$

$$-\int_{\Gamma_B} \delta(\boldsymbol{\sigma} \cdot \mathbf{n}) \cdot \boldsymbol{\psi}_u \, d\Gamma \, dt + \frac{\partial I_c}{\partial \mathbf{u}} \delta \mathbf{u} + \frac{\partial I_c}{\partial p} \delta p = \mathbf{0} \text{ on } \Gamma_B \quad (16)$$

where,  $\mathbf{s} = \{\mathbf{u}\boldsymbol{\psi}_u - \psi_p + \mu[\nabla\boldsymbol{\psi}_u + (\nabla\boldsymbol{\psi}_u)^T]\} \cdot \mathbf{n}$ .  $\Gamma_U$ ,  $\Gamma_D$  and  $\Gamma_S$  are the upstream, downstream and lateral boundaries and  $\Gamma_B$  is the body surface (see Figure 1). We observe that the boundary conditions on the adjoint variables, on the surface of the body, depend on the definition of the objective function.

#### 2.4 Multi-point objective function

The multi-point objective function is defined using the weighted-sum method. Let  $N_{dp}$  be the number of design points,  $I_i$  the objective function at the  $i^{th}$  point and  $w_i$  its user-defined weight.  $I_i$  is the augmented objective function given by Equation (6). The cumulative objective function is defined as:

$$I = \sum_{i=1}^{N_{dp}} w_i I_i. \quad (17)$$

The gradient, for the multi-point objective function, is given by:

$$\frac{\partial I}{\partial \boldsymbol{\beta}} = \sum_{i=1}^{N_{dp}} w_i \left( \frac{\partial I_i}{\partial \boldsymbol{\beta}} \right). \quad (18)$$

### 3 Finite element formulation

#### 3.1 The flow equations

The domain  $\Omega$  is discretized into elements  $\Omega^e$ ,  $e = 1, 2, \dots, n_{el}$ , where  $n_{el}$  is the number of elements. Let  $\mathcal{S}_u^h$  and  $\mathcal{S}_p^h$  be the appropriate finite element spaces and  $\mathcal{V}_u^h$  and  $\mathcal{V}_p^h$  the weighing function spaces for velocity and pressure, respectively. The stabilized finite element formulation of Equations (1) and (2) is written as

follows: find  $\mathbf{u}^h \in \mathcal{S}_u^h$  and  $p^h \in \mathcal{S}_p^h$  such that  $\forall \mathbf{w}^h \in \mathcal{V}_u^h, q^h \in \mathcal{V}_p^h,$

$$\begin{aligned} & \int_{\Omega} \mathbf{w}^h \cdot \rho \mathbf{u} \cdot \nabla \mathbf{u} \, d\Omega + \int_{\Omega} \varepsilon(\mathbf{w}^h : \boldsymbol{\sigma}(p^h, \mathbf{u}^h)) \, d\Omega \\ & + \int_{\Omega} q^h \nabla \cdot \mathbf{u}^h \, d\Omega + \sum_{e=1}^{n_{el}} \int_{\Omega^e} \frac{1}{\rho} (\tau_{SUPG} \rho \mathbf{u}^h \cdot \nabla \mathbf{w}^h + \tau_{PSPG} \nabla q^h) \cdot \\ & [\rho \mathbf{u} \cdot \nabla \mathbf{u} - \nabla \cdot \boldsymbol{\sigma}] \, d\Omega^e \\ & + \sum_{e=1}^{n_{el}} \int_{\Omega^e} \tau_{LSIC} \nabla \cdot \mathbf{w}^h \rho \nabla \cdot \mathbf{u}^h \, d\Omega^e = \int_{\Gamma^h} \mathbf{w}^h \cdot \mathbf{h}^h \, d\Gamma. \end{aligned} \tag{19}$$

The first three terms and the right-hand side in the variational formulation given by Equation (19) constitute the Galerkin formulation of the problem. The terms involving the element level integrals are the stabilization terms added to the basic Galerkin formulation to enhance its numerical stability. These terms stabilize the computations against node-to-node oscillations in advection dominated flows and allow the use of equal-in-order basis functions for velocity and pressure. The terms with coefficients  $\tau_{SUPG}$  and  $\tau_{PSPG}$  are based on the SUPG (Streamline-Upwind/Petrov-Galerkin) and PSPG (Pressure-stabilized/Petrov-Galerkin) method [Tezduyar, Mittal, Ray, and Shih (1992)]. The term with coefficient  $\tau_{LSIC}$  is also a stabilization term based on the least squares of the incompressibility constraint and is found to be useful for large Reynolds number flows. Equal-in-order basis functions for velocity and pressure, that are linear in space (three-noded triangular elements) are used. A three point quadrature is employed for numerical integration. This approach, based on the finite element method, has been successfully applied to solving various fluid flow problems. In three dimensions, it is sometimes difficult to generate well-resolved meshes for complex geometries. Meshless methods provide a nice framework to deal with such situations. According to Atluri and Zhu [Atluri and Zhu (2000)], the main objective of meshless methods is to get rid of or at least alleviate the difficulty of meshing and remeshing the entire structure, by only adding or deleting nodes in the entire structure. A number of meshless methods have been developed. Some examples are the element free Galerkin method [Belytschko, Organ, and Y.Krongauz (1994)], reproducing kernel particle method [Liu, Chen, Chang, and Belytschko (1996)], meshless local boundary equation (MLBIE) method [Zhu, Zhang, and Atluri (1998)] and meshless local Petrov-Galerkin method (MLPG) [Atluri and Zhu (1998, 2000); Atluri and Shen (2002); Atluri, Han, and Rajendran (2003)]. Lin and Atluri [Lin and Atluri (2002)] compared the SUPG and MLPG approaches for convection diffusion problems and found them to provide comparable results.

### 3.2 The adjoint equations

A stabilized SUPG/PSPG finite element method is proposed to solve the adjoint equations (11) and (12). Let  $\mathcal{S}_{\psi_u}^h$  and  $\mathcal{S}_{\psi_p}^h$  be the appropriate finite element spaces and  $\mathcal{V}_{\psi_u}^h$  and  $\mathcal{V}_{\psi_p}^h$  the corresponding weighting function spaces for the adjoint velocity and adjoint pressure. The stabilized finite element formulation of Equations (11) and (12) is written as follows: given  $\mathbf{u}^h$  and  $\mathbf{p}^h$  satisfying Equations (1) and (2), find  $\psi_u^h \in \mathcal{S}_{\psi_u}^h$  and  $\psi_p^h \in \mathcal{S}_{\psi_p}^h$  such that  $\forall \mathbf{w}_{\psi_u}^h \in \mathcal{V}_{\psi_u}^h, q_{\psi_p}^h \in \mathcal{V}_{\psi_p}^h$ ,

$$\begin{aligned} & \int_{\Omega} \mathbf{w}_{\psi_u}^h \cdot \rho \left( (\nabla \mathbf{u}^h)^T \psi_u^h - \mathbf{u} \cdot \nabla \psi_u^h \right) d\Omega + \int_{\Omega} \varepsilon(\mathbf{w}_{\psi_u}^h) : \boldsymbol{\sigma}_{\psi}(\psi_p^h, \psi_u^h) d\Omega \\ & + \int_{\Omega} q_{\psi_p}^h \nabla \cdot \psi_u^h d\Omega + \sum_{e=1}^{n_{el}} \int_{\Omega^e} \frac{1}{\rho} \left( -\tau_{SUPG} \rho \mathbf{u}^h \cdot \nabla \mathbf{w}_{\psi_u}^h + \tau_{PSPG} \nabla q_{\psi_p}^h \right) \\ & \left[ \rho \left( (\nabla \mathbf{u}^h)^T \psi_u^h - \mathbf{u} \cdot \nabla \psi_u^h \right) - \nabla \cdot \boldsymbol{\sigma}_{\psi}(\psi_p^h, \psi_u^h) \right] d\Omega^e \\ & + \sum_{e=1}^{n_{el}} \int_{\Omega^e} \tau_{LSIC} \nabla \cdot \mathbf{w}_{\psi_u}^h \rho \nabla \cdot \psi_u^h d\Omega^e = 0. \end{aligned} \quad (20)$$

The stabilization coefficients  $\tau_{SUPG}$ ,  $\tau_{PSPG}$  and  $\tau_{LSIC}$  in the formulation proposed in equation (20) are computed based on the flow variables  $(\mathbf{u}, p)$ .

## 4 Parametrization

The choice of design variables depends on the parametrization used to represent the surface. One would like to use a parametrization that offers a rich design space. At the same time, too many degrees of freedoms can lead to a noisy shape that is associated with problems related to mesh generation. In the present work, NURBS (Non-Uniform Rational B-Splines) [Farin (1990)] have been used to parametrize the airfoil geometry. Figure 2 shows the representation of NACA 0012 airfoil at  $\alpha = 0^\circ$  with 13 control points. The control polygon is also shown. The control points comprising of the trailing and leading edges are held fixed to maintain pre-assigned chord length and angle of attack. The y-coordinates of the remaining control points are used as design variables. Each design variable is allowed to move between a lower and upper bound which have been set to avoid unacceptable shape distortions.

## 5 The optimizer

The optimization algorithm used in the present work is the L-BFGS (Limited memory-Broyden-Fletcher-Goldfarb-Shanno) procedure [Byrd, Lu, Nocedal, and Zhu (1995)].

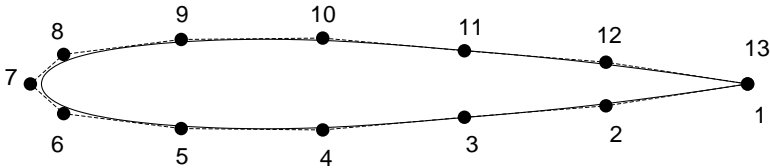


Figure 2: Parametrization of a NACA0012 airfoil with NURBS curve using 13 control points. Points 1, 7 and 13 are held fixed while the  $y$ -coordinates of the remaining control points are used as design variables.

This is a limited memory quasi-Newton method for solving large nonlinear optimization problems that are constrained by upper and lower bounds on the design variables. The algorithm is well suited for problems when the information for the second derivative (the Hessian) is difficult to obtain.

## 6 Algorithm

The algorithm for the design procedure is as follows:

1. Begin with an initial geometry and generate the finite element mesh.
2. Compute flow variables  $\mathbf{u}$  and  $p$  using Equation 19.
3. Compute adjoint variables  $\boldsymbol{\psi}_{\mathbf{u}}$  and  $\boldsymbol{\psi}_p$  using Equation 20.
4. Compute the gradient using Equation 10.
5. Repeat steps 2, 3 and 4 for  $N_{dp}$  sampling points.
6. Compute the multi-point objective function and its gradient using Equations 17 and 18, respectively.
7. Pass the gradient information to the optimizer and update the shape/design parameters  $\boldsymbol{\beta}$ .
8. Modify the finite element mesh to accommodate the new shape. A mesh moving scheme is used in the present work.
9. Repeat the above till the condition for convergence, either on the gradient or objective function, is satisfied.

## 7 Results

Multi-point optimization is carried out for two cases. The first involves an inverse objective function on the lift coefficient at a specific angle of attack of the airfoil over a range of  $Re$ . The second case involves a direct objective function over a range of angles of attack. In this case the  $Re$  is held constant. The mesh used for both the computations is same. A close-up view of a sample mesh generated over the NACA0012 airfoil at  $\alpha = 0^\circ$  is shown in Figure 3. It has 9828 nodes and 19406 triangular elements with 200 nodes on the surface. A structured mesh is used near the surface while an unstructured mesh, obtained via Delaunay triangulation, is generated in the rest of the domain.

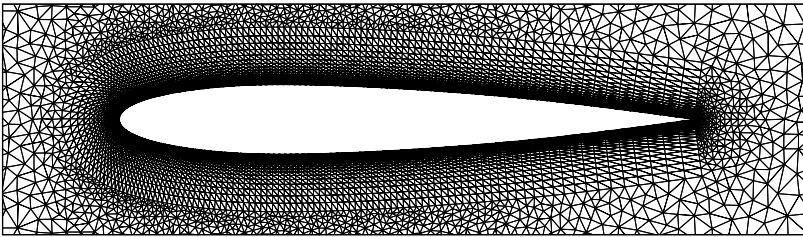


Figure 3: Close-up view of a sample mesh. It has 9828 nodes and 19406 triangular elements with 200 nodes on the surface.

### 7.1 Multi-point design at different $Re$

The objective is to design an airfoil with  $C_l = 0.4$  at three values of  $Re$ : 10, 100 and 500. The angle of attack is fixed at  $\alpha = 4^\circ$ . The objective function to be minimized is given as:

$$I_c = w_1 I_{c_1}|_{Re=10} + w_2 I_{c_2}|_{Re=100} + w_3 I_{c_3}|_{Re=500} \quad (21)$$

where  $w_1$ ,  $w_2$  and  $w_3$  are weights corresponding to the objective function at the respective  $Re$ .  $I_{c_i}$  is defined as

$$I_{c_i} = \frac{1}{2} (C_l - 0.4)^2 \quad i = 1, 2, 3 \quad (22)$$

In the present computations,  $w_1$ ,  $w_2$  and  $w_3$  are all set to 1.0. The NACA 0012 airfoil at  $\alpha = 4^\circ$  is used as the initial guess. Figures 4(a) and (b) show the variation of

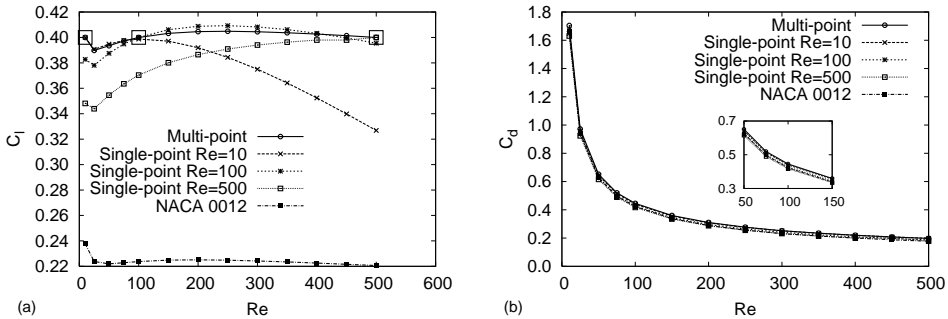


Figure 4: Multi-point shape design of airfoil having  $C_l = 0.4$  at  $Re = 10, 100$  and  $500$  at  $\alpha = 4^\circ$ : variation of (a)  $C_l$  and (b)  $C_d$  with  $Re$  of the optimal shape along with those of single-point optimal design and NACA 0012 airfoils.

the lift and drag coefficient, respectively, for the NACA 0012 airfoil with  $Re$ . As expected,  $C_d$  shows a monotonic decrease with  $Re$  while  $C_l$  exhibits a non-monotonic behavior at  $Re \sim 50$ . This is caused by the fact that the pressure contribution to  $C_l$  decreases while the viscous contribution increases with increase in  $Re$ . Further details can be found in the work by Srinath and Mittal [Srinath and Mittal (2009)].

Figure 5(a) shows the final shape obtained at the end of the design cycle. The optimal airfoil is seen to have a thick and rounded leading edge and a large 'dimple' at, approximately, the quarter chord section. The lower surface is almost flat. The pressure distribution over the NACA 0012 and the optimal airfoil is shown in the first and second columns of of Figure 6 at  $Re = 10, 100$  and  $500$ , respectively. The optimal airfoil, at all the  $Re$ , has a larger peak suction on the upper surface as compared to the NACA 0012 airfoil. Also the pressure on the lower surface is larger for the optimal airfoil. This leads to increased lift generated by the optimal airfoil. The iteration history of the objective function and the  $L_2$  norm of the gradient are shown in Figures 7(a) and (b). 25 iterations are required for the objective function to satisfy the convergence criteria which, in this case, is specified as achieving the  $L_2$  norm of gradient below  $10^{-5}$ .

Since one of the primary motive of carrying out multi-point design is to improve off-design performance, flow over the optimal airfoil is computed for various  $Re$ . Figure 4 shows the variation of the lift and drag coefficients of the optimal airfoil with respect to  $Re$ . The various  $Re$  at which shape optimization is carried out are also marked in the figure, for reference. The optimal airfoil has  $C_l < 0.4$  for  $10 \leq Re \leq 100$ . It produces slightly larger  $C_l$  for  $100 < Re \leq 500$ .

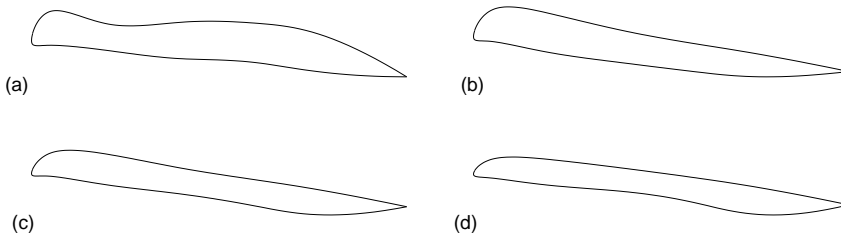


Figure 5: Inverse design of airfoil with  $C_l = 0.4$  at  $\alpha = 4^\circ$ : (a) multi-point design (at  $Re = 10, 100$  and  $500$ ) and single point design at (b)  $Re = 10$ , (c)  $Re = 100$  and (d)  $Re = 500$ .

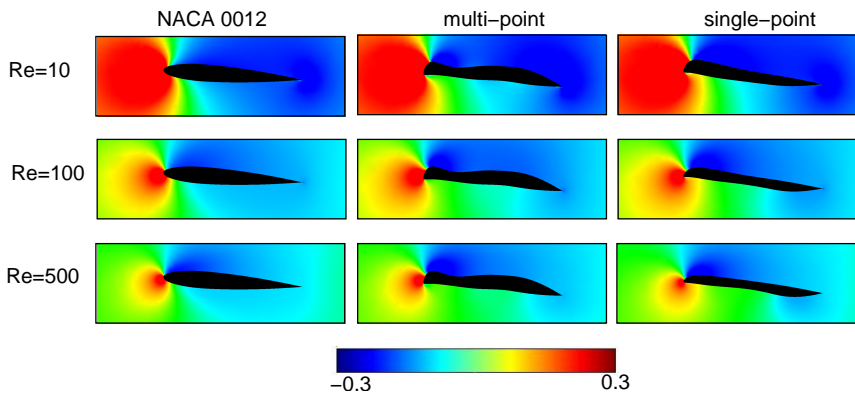


Figure 6: Inverse design of airfoil having  $C_l = 0.4$ : pressure distribution over NACA 0012 and optimal airfoils from multi-point and single-point design at  $\alpha = 4^\circ$ .

### 7.1.1 Single-point versus multi-point design

In this section the performance of single- and multi-point design are compared. Optimal shapes are obtained for single-point designs at  $Re = 10, 100$  and  $500$  for  $C_l = 0.4$ . The single-point optimal shapes are shown in Figures 5(b), (c) and (d). It is seen that the airfoil obtained from the multi-point design is significantly different from that of single-point design. Pressure distribution for these airfoils at their design  $Re$  are shown in Figure 6.

The variation of  $C_l$  with respect to  $Re$  for each of the single-point optimal shapes is shown in Figure 4. The optimal airfoil at  $Re = 10$  has  $C_l = 0.4$  at its designated  $Re$ . However, it produces lesser lift with increasing  $Re$ . The optimal airfoil at  $Re = 100$

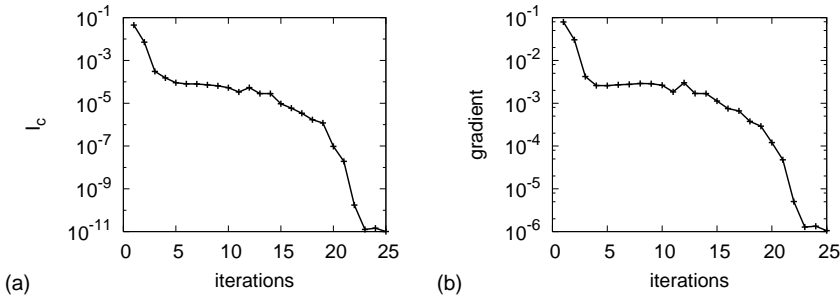


Figure 7: Multi-point design of an airfoil having  $C_l = 0.4$  at  $Re = 10, 100$  and  $500$ : iteration history of (a) objective function,  $I_c$  and (b)  $L_2$  norm of the gradient. The angle of attack is  $4^\circ$ .

has  $C_l$  lesser than its design value of  $0.4$  at  $Re < 100$  but shows an increasing trend beyond  $Re = 25$ . At  $Re = 500$  this airfoil produces slightly lesser lift than the designated  $C_l$ . The optimal airfoil at  $Re = 500$  produces substantially lesser lift at lesser  $Re$ . In comparison, the multi-point airfoil, while matching its design requirements, has a better off-design performance.

## 7.2 Multi-point design at different $\alpha$

The objective in this case is to determine an airfoil that has the largest lift coefficient at various angles of attack at  $Re = 500$ . Three angles of attack are considered:  $\alpha = 4^\circ, 8^\circ$  and  $12^\circ$ . The objective function is given by

$$I_c = w_1 I_{c_1}|_{\alpha=4^\circ} + w_2 I_{c_2}|_{\alpha=8^\circ} + w_3 I_{c_3}|_{\alpha=12^\circ} \quad (23)$$

As in the previous case, weights  $w_1, w_2$  and  $w_3$  are set to  $1.0$ . In the above expression,  $I_{c_i}$  is given by

$$I_{c_i} = -\frac{1}{2} C_l^2 \quad i = 1, 2, 3 \quad (24)$$

Figure 8(a) shows the final shape obtained at the end of the design cycle. The optimal airfoil is seen to be a curved plate. Figure 9(a) shows the variation of  $C_l$  with respect to  $\alpha$  for the optimal airfoil. The optimal airfoil generates  $159\%$ ,  $103\%$  and  $85\%$  more lift than the NACA 0012 airfoil at  $\alpha = 4^\circ, 8^\circ$  and  $12^\circ$ , respectively. The pressure distribution over NACA 0012 and the optimal airfoil are shown in the first and second columns of Figure 10, respectively. An extended region of higher pressure exists on the lower surface at all the three angles of attack studied.

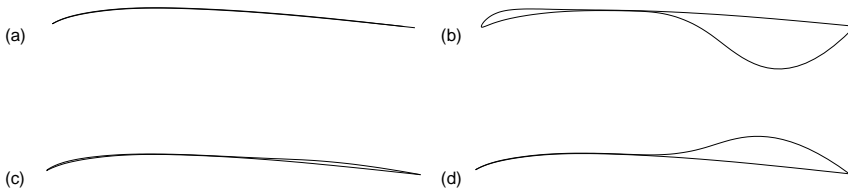


Figure 8: Maximization of lift coefficient at  $Re = 500$ : optimal shapes obtained with (a) multi-point design at  $\alpha = 4^\circ, 8^\circ$  and  $12^\circ$  (b) single point design at (b)  $\alpha = 4^\circ$ , (c)  $8^\circ$  and (d)  $12^\circ$ .

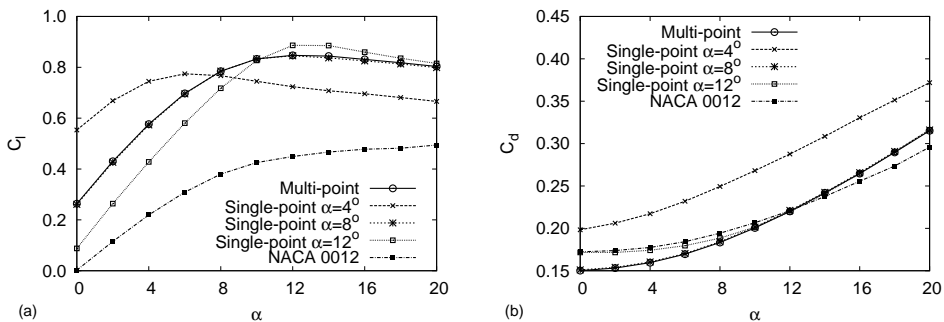


Figure 9: Maximization of lift coefficient at  $\alpha = 4^\circ, 8^\circ, 12^\circ$  and  $Re = 500$ : variation of (a)  $C_l$  and (b)  $C_d$  with  $Re$  of the optimal shape along with those of single-point optimal design and NACA 0012 airfoils.

### 7.2.1 Single-point vs multi-point design

As in the previous case, the optimal airfoil obtained with multi-point design is compared with those obtained from single-point design. The optimal airfoils obtained for maximum lift at  $\alpha = 4^\circ, 8^\circ, 12^\circ$  are shown in Figures 8(b), (c) and (d), respectively. The single-point optimal airfoil obtained at  $\alpha = 4^\circ$  has a large bulge on the lower rear surface while at  $12^\circ$  the bulge shifts to the upper rear surface. The airfoil obtained at  $8^\circ$  is very similar to the multi-point optimal airfoil. The pressure distribution over the single-point optimal airfoils are shown in the third column of Figure 10. The optimal airfoil at  $\alpha = 4^\circ$  has a high pressure region on the lower surface owing to the bulge. The variation of  $C_l$  and  $C_d$  with respect to  $\alpha$  for the optimal airfoils are shown in Figure 9. As expected, the single-point designed airfoils have

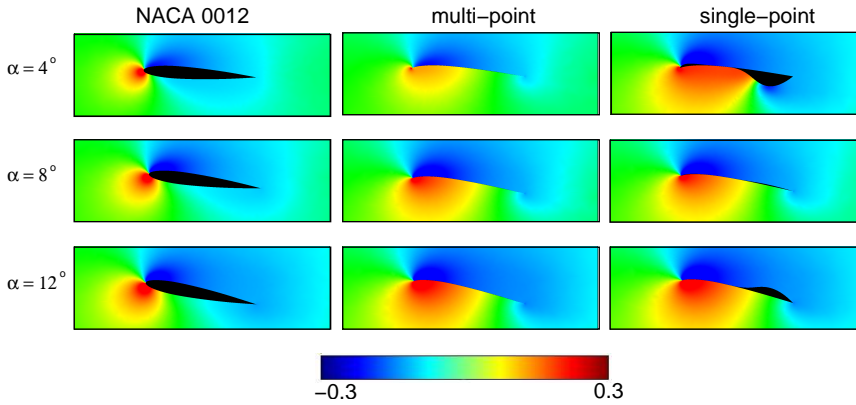


Figure 10: Maximization of lift coefficient at  $Re = 500$ : pressure distribution over NACA 0012 and optimal airfoils obtained from multi-point and single-point design at  $\alpha = 4^\circ, 8^\circ, 12^\circ$ .

their optimum performance at their design angle of attack. In general, at the design points, their performance is marginally superior to the performance of airfoil from the multi-point design. However, at off-design conditions, the loss of performance of the multi-point design is much less than that of the single-point design. The multi-point design airfoil produces almost the same lift as the single-point design airfoils at  $\alpha = 8^\circ$  and  $12^\circ$ . At  $4^\circ$  the multi-point designed airfoil has a  $C_l$  that is 22% lesser than the single-point design airfoil while at  $12^\circ$  its  $C_l$  is only 4% smaller than the single-point design at the corresponding  $\alpha$ . The uneven difference at various  $\alpha$  is because the contribution to the objective function, given by Equation 23, from the various sampling points is not of the same magnitude. The contribution from the  $12^\circ$  computation is more than that of the  $4^\circ$ . Therefore, the optimizer tends to look for optimal solutions in the direction of the largest contributor to the objective function. This can be overcome by suitably weighing the different terms so that their contribution is similar in magnitude. This, however, has not been undertaken in the present study. Optimizing the weights themselves is an exercise that will be taken up in a future study.

## 8 Conclusions

A continuous adjoint method for multi-point shape optimization of airfoils at low  $Re$  has been formulated and implemented. A stabilized finite element method based on SUPG/PSPG stabilization has been used to solve, both, flow and adjoint equations. The airfoil is parametrized by a 4<sup>th</sup> order NURBS curve with 13 control

points. The  $y$  coordinates of control points are used as the design variables. NACA 0012 airfoil is used as the initial guess in all the computations.

Two different objective functions are studied for the multi-point optimal design of an airfoil. The first objective function is an inverse function on the lift coefficient. The objective is to find a shape having lift coefficient of 0.4 at  $Re = 10, 100$  and  $500$ . The angle of attack is  $4^\circ$ . The final shape is seen to have a rounded leading edge with a large 'dimple' around the quarter chord section. This shape is compared with optimal airfoil shapes obtained individually at  $Re = 10, 100$  and  $500$ . The multi-point shape is found to be significantly different from the optimal single-point shapes. The variation of the lift coefficient with respect to the  $Re$  is plotted for each of these shapes. It is noticed that the single point designs perform optimally at their operation condition and have an inferior off design performance. On the other hand, the optimal multi-point design, while satisfying its design requirement, has a better off-design performance.

The second objective function is to maximize the lift coefficient at  $\alpha = 4^\circ, 8^\circ$  and  $12^\circ$ . The  $Re$  is  $500$ . The optimal shape obtained is a thin curved plate. This airfoil produces 159%, 103% and 85% more lift than the NACA 0012 airfoil at the considered  $\alpha$ . Single-point designs are computed for these angles of attack. The multi-point optimal shape is seen to be similar to that obtained from single-point design at  $\alpha = 8^\circ$ . The multi-point airfoil generates 22% and 4% lesser lift compared to the corresponding single-point design airfoils at  $\alpha = 4^\circ, 12^\circ$ . This difference arises because the weights assigned to each of the terms in the objective function is same, irrespective of the individual contribution to it. The off-design performance of the multi-point design is superior to that of single-point design. For the reasons that have been pointed out, the performance of the multi-point design is better at larger  $\alpha$ .

## References

**Abraham, F.; Behr, M.; Heinkenschloss, M.** (2005): Shape optimization in steady blood flow: A numerical study of non-Newtonian effects. *Computer Methods in Biomechanics and Biomedical Engineering*, vol. 8, pp. 127–137.

**Anderson, W.; Bonhaus, D.** (1999): Airfoil design on unstructured grids for turbulent flows. *AIAA Journal*, vol. 36, pp. 185–191.

**Anderson, W. K.; Venkarakrishnan, V.** (1997): Aerodynamic design optimization on unstructured grids with a continuous adjoint formulations. AIAA Paper 97-0643, 1997.

**Atluri, S.; Han, Z.; Rajendran, A.** (2003): A new implementation of the meshless finite volume method, through the MLPG mixed approach. *CMES: Computer Modelling in Engineering and Sciences*, vol. 4, pp. 507–517.

**Atluri, S.; Shen, S.** (2002): The meshless local Petrov-Galerkin (MLPG) method: A simple and less-costly alternative to the finite element and boundary element methods. *CMES: Computer Modelling in Engineering and Sciences*, vol. 3, pp. 11–51.

**Atluri, S.; Zhu, T.** (1998): A new meshless local Petrov-Galerkin approach in computational mechanics. *Computational Mechanics*, vol. 22, pp. 117–127.

**Atluri, S.; Zhu, T.** (2000): New concepts in meshless methods. *International Journal For Numerical Methods In Engineering*, vol. 47, pp. 537–556.

**Belytschko, T.; Organ, D.; Y.Krongauz** (1994): A coupled finite element-free Galerkin method. *International Journal For Numerical Methods In Engineering*, vol. 17, pp. 186–195.

**Bendsoe, M.; Kikuchi, N.** (1988): Generating optimal topology in structural design using a homogenization method. *Computer Methods in Applied Mechanics and Engineering*, vol. 71, pp. 197–224.

**Bendsoe, M.; Sigmund, O.** (1999): Material interpolation schemes in topology optimization. *Archives in applied mechanics*, vol. 69, pp. 635–654.

**Bendsoe, M.; Sigmund, O.** (2002): *Topology Optimization: Theory, Methods and Applications*. Springer-Verlag, Berlin.

**Brezillion, J.; Gauger, N.** (2004): 2D and 3D aerodynamic shape optimization using the adjoint approach. *Aerospace Science and Technology*, vol. 8, pp. 715–727.

**Burg, C.; Newman, J.** (2003): Computationally efficient, numerically exact design derivatives via the complex Taylor series expansion method. *Computers and Fluids*, vol. 32, pp. 373–383.

**Byrd, R.; Lu, P.; Nocedal, J.; Zhu, C.** (1995): A limited memory algorithm for bound constrained optimization. *SIAM Journal of Scientific Computing*, vol. 16, pp. 1190–1208.

**Cisilino, A.** (2006): Topology optimization of 2D potential problems using boundary elements. *CMES: Computer Modelling in Engineering and Sciences*, vol. 15, pp. 99–106.

- Drela, M.** (1998): Pros & cons of airfoil optimization. In Caughey, D.; Hafeez, M.(Eds): *Frontiers of computational fluid dynamics*, pp. 363–381. World scientific, Singapore.
- Elliot, J.; Perraire, J.** (1997): Practical three-dimensional design and optimization using unstructured meshes. *AIAA Journal*, vol. 35, pp. 1479–1485.
- Farin, G.** (1990): *Curves and Surfaces for Computer Aided Geometric Design. A Practical Guide*. Academic Press.
- Hou, G.; Sheen, J.; Chuang, C.** (1992): Shape sensitivity analysis and design optimization of linear thermoelastic solids. *AIAA Journal*, vol. 30, pp. 528–537.
- Huyse, L.; Padula, S.; Lewsi, R.; Li, W.** (2002): Probabilistic approach to free-form airfoil shape optimization under uncertainty. *AIAA Journal*, vol. 40, pp. 1764–1772.
- Jameson, A.** (1988): Aerodynamic design via control theory. *Journal of Scientific Computing*, vol. 59, pp. 117–128.
- Juan, Z.; Shuyao, L.; Yuanbo, X.; Guangyao, L.** (2008): A topology optimization design for the continuum structure based on the meshless numerical technique. *CMES: Computer Modelling in Engineering and Sciences*, vol. 34, pp. 137–154.
- Kim, S.; Alonso, J.; Jameson, A.** (2000): Two-Dimensional high lift aerodynamic optimization using the continuous adjoint method. *AIAA Paper 2000-4741*, 2000.
- Li, W.; Huyse, L.; Padula, S.** (2002): Robust airfoil optimization to achieve drag reduction over a range of Mach numbers. *Structural and multidisciplinary optimization*, vol. 24, pp. 38–50.
- Lin, H.; Atluri, S.** (2002): Meshless local Petrov-Galerkin (MLPG) method for convection-diffusion problems. *CMES: Computer Modelling in Engineering and Sciences*, vol. 1, pp. 45–60.
- Liu, C.; Atluri, S.** (2008): A fictitious time integration method (*ftim*) for solving mixed complementarity problems with applications to nonlinear optimization. *CMES: Computer Modelling in Engineering and Sciences*, vol. 35, pp. 155–178.
- Liu, W.; Chen, Y.; Chang, C.; Belytschko, T.** (1996): Advances in multiple scale kernel particle methods. *Computational Mechanics*, vol. 18, pp. 73–111.
- M.B.Giles; Pierce, N.** (2000): An introduction to the adjoint approach to design. *Flow, Turbulence and Combustion*, vol. 65, pp. 393–415.

**Mohammadi, B.** (2004): Optimization of aerodynamic and acoustic performances of supersonic civil transports. *International Journal For Numerical Methods In Fluids*, vol. 14, pp. 891–907.

**Mohammadi, B.; Pirroneau, O.** (2004): Shape optimization in fluid mechanics. *Annual Review of Fluid Mechanics*, vol. 36, pp. 255–279.

**Nemec, M.; Zingg, D.; Pulliam, T.** (2004): Multipoint and multi-objective aerodynamic shape optimization. *AIAA Journal*, vol. 42, pp. 1057–1065.

**Obyashi, S.** (1996): Aerodynamic inverse optimization with genetic algorithms. *Journal of Engineering and Applied Science*, pp. 421–425.

**Okumura, H.; Kawahara, M.** (2000): Shape optimization of a body located in incompressible Navier-Stokes flow based on optimal control theory. *CMES: Computer Modelling in Engineering and Sciences*, vol. 1, pp. 71–77.

**Pirroneau, O.** (1973): On optimum profiles in Stokes flow. *Journal of Fluid Mechanics*, vol. 59, pp. 117–128.

**Pirroneau, O.** (1974): On optimum design in fluid mechanics. *Journal of Fluid Mechanics*, vol. 64, pp. 97–110.

**Sherman, L.; Taylor, V.; Green, L.; P.A.Newman; Hou, G.; Korivi, M.** (1994): First and second order aerodynamic sensitivity derivatives via automatic differentiation with incremental iterative methods. *Journal of Computational Physics*, vol. 129, pp. 307–331.

**Soto, O.; Lohner, R.; Yang, C.** (2004): An adjoint-based design methodology for CFD problems. *International Journal of Numerical Methods for Heat and Fluid Flow*, vol. 14, pp. 734–759.

**Srinath, D.; Mittal, S.** (2009): Optimal airfoil shapes for low reynolds number flows. *International Journal For Numerical Methods In Fluids*, vol. 61, pp. 355–381.

**Tapp, C.; Hansel, W.; Mittelstedt, C.; Becker, W.** (2004): Weight-minimization of sandwich structures by a heuristic topology optimization algorithm. *CMES: Computer Modelling in Engineering and Sciences*, vol. 5, pp. 563–574.

**Tezduyar, T.; Mittal, S.; Ray, S.; Shih, R.** (1992): Incompressible flow computations with stabilized bilinear and linear equal order interpolation velocity pressure elements. *Computer Methods in Applied Mechanics and Engineering*, vol. 95, pp. 221–242.

**Wang, S.; Lim, K.; Khoo, B.; Wang, M.** (2007): A geometric deformation constrained level set method for structural shape and topology optimization. *CMES: Computer Modelling in Engineering and Sciences*, vol. 18, pp. 155–181.

**Zhou, M.; Rozvany, G.** (2001): On the validity of ESO type methods in topology optimization. *Structural and multidiscipline optimization*, vol. 21, pp. 83–101.

**Zhu, T.; Zhang, J.; Atluri, S.** (1998): A local boundary equation (LBIE) approach in computational mechanics and a meshless discretization approach. *Computational Mechanics*, vol. 21, pp. 223–235.

**Zingg, D.; Elias, S.** (2006): Aerodynamic shape optimization under a range of operating conditions. *AIAA Journal*, vol. 44, pp. 2787–2792.

